Towards Scanning Tunneling Microscopy Measurements on Micrometer-Sized Graphene Flakes.

THESIS

submitted in partial fulfillment of the
requirements for the degree of

MASTER OF SCIENCE
in
PHYSICS

Author :	Tjerk Benschop
Student ID :	1406035
Supervisor :	Prof. Dr. M.P. Allan
2^{nd} corrector :	Prof. Dr. J.M. van Ruitenbeek

Leiden, The Netherlands, November 25, 2018

Towards Scanning Tunneling Microscopy Measurements on Micrometer-Sized Graphene Flakes.

Tjerk Benschop

Leiden Institute of Physics
P.O. Box 9500, 2300 RA Leiden, The Netherlands

November 25, 2018

Abstract

Motivated by the recent discovery of superconductivity in Magic Angle Twisted Bilayer Graphene, we discuss preparatory work for STM measurements on micrometer-sized graphene flakes. We develop and fabricate a dummy sample for testing capacitive navigation in any STM setup with an XY-stage. Furthermore, we calculate the effect of a biased STM tip on the charge distribution in a graphene bilayer. We also estimate the chemical potential shift in a gated graphene sample as a result of the probe tip. All results unambiguously suggest that the STM tip will strongly influence the electrical behavior of the graphene system.

Contents

Version of November 25, 2018– Created November 25, 2018 - 02:09

Chapter 1

Introduction

In this work, we describe the first steps towards Scanning Tunneling Microscopy (STM) measurements on micrometer-sized graphene flakes. Motivated by the recent discovery of superconductivity in so called Magic Angle Twisted Bilayer Graphene (MA-TBG) [1, 2], we investigate the possibility of doing STM measurements on flakes of bilayer graphene on hexagonal Boron Nitride.
STM measurements would allow us to study the emergent superconductivity on the atomic scale. Unfortunately, STM also has a disadvantage hidden in its core mechanic when it comes to studying low-density free carrier materials: due to extremely small distance between them, the charge dynamics in the sample can be influenced by the electric field emitted by the tip. Although this effect is often ignored, because free carriers in the sample often screen the field emitted by the tip, as a result of the low free carrier density of graphene ($\sim 10^{12}$), unfortunately, this effect can be quite substantial in this material. In this work, we attempt to calculate the charge distribution in a graphene bilayer as a result of a biased probe in proximity to the bilayer.
Another challenge when it comes to studying graphene flakes with STM, is landing the probe tip on the sample. To overcome this, most researchers study graphene in a system with optical access to the STM. Unfortunately, in most low-temperature setups, optical access is not available. To overcome this we investigate capacitive navigation of the probe tip to the sample. We demonstrate the fabrication of a dummy sample for testing a capacitive navigation protocol. Unfortunately, because a functioning STM setup was unavailable during the time span of this master project, we could not actually test this technique yet.

Version of November 25, 2018– Created November 25, 2018 - 02:09

Chapter 2

Graphene

* Graphene consists of carbon atoms forming the well known honeycomb lattice with a lattice constant of 2.46Å (figure 2.1a). The band structure of this system can be deduced rather easily by following the tight-binding approach [3, 4]. Each carbon atom contributes 4 electrons to the system. Three of those form strong covalent bonds with the nearest neighboring carbon atoms and therefore do not play any major role in transport. The fourth one, however, occupies the p_z orbital and does contribute to transport. For this reason, graphene can be modeled as a hexagonal lattice with a two atom basis in which each atom contributes one free electron.

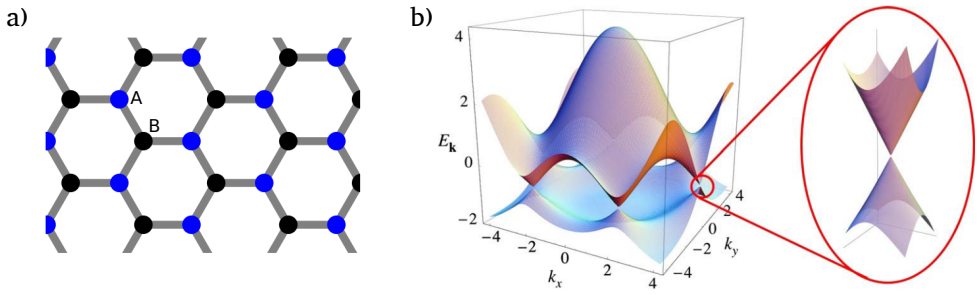

Figure 2.1: *a) Crystal lattice of graphene. The crystal consists of a two-atom basis in a hexagonal lattice. The individual atoms that form the basis are referred to as A (blue) and B (black). b) Band structure of graphene as calculated by the tight binding model [3, 4]. The inset shows a magnifications of one of the six points where the upper and lower bands touch, forming a Dirac cone. Image from reference [4].*

*This chapter was partially copied from my earlier work: Visualizing Strongly Correlated Electronic States in Bilayer Graphene with a Scanning Tunneling Microscope

Following the tight-binding approach, the dispersion relation can be calculated:

$$\begin{aligned} E(\mathbf{k}) &= \pm t\sqrt{3+f(\mathbf{k})} - t'f(\mathbf{k}), \text{ where} \\ f(\mathbf{k}) &= 2\cos\left(\sqrt{3}k_y a\right) + 4\cos\left(\frac{3}{2}k_x a\right)\cos\left(\frac{\sqrt{3}}{2}k_y a\right). \end{aligned} \tag{2.1}$$

In this expression, a is the distance between nearest neighboring carbon atoms (1.42Å), and t, t' are the hopping amplitudes corresponding to hopping between nearest neighboring (A to B, figure 2.1a), and next nearest neighboring (A to A) atoms respectively. Figure 2.1b shows the calculated dispersion relation. This tight-binding dispersion can be expanded around the K and K′ points ($\frac{2\pi}{3a}\left(1, \frac{1}{\sqrt{3}}\right)$ and $\frac{2\pi}{3a}\left(1, \frac{-1}{\sqrt{3}}\right)$ respectively), yielding a linear dispersion for small momentum displacement ($E \sim v_F|\mathbf{k}|$, v_F is the Fermi velocity). These areas of momentum space are known as Dirac cones. The reason for this is that this linear dispersion relation quantum mechanically describes relativistic particles known as Dirac fermions [5]. Note that these are in essence very different from ordinary electrons; since there is no effective mass term present in the dispersion relation. The presence of relativistic Dirac fermions has experimentally been confirmed by measuring the $\sqrt{n}$ dependence of the cyclotron mass [4].

Stacking graphene: A route to induce strong correlations
When stacking two sheets of graphene on top of each other, interlayer hopping needs to be considered, and as a consequence, the electronic structure of the sheets changes. Depending on the stacking order (AA or AB), the band structure differs quite substantially due to a different interlayer hopping magnitude [6]. When two sheets are stacked under an angle with respect to each other, a so called Moiré pattern forms (figure 2.2). This Moiré superlattice consists of alternating AA and AB stacked zones. As a result of this, the original periodicity of the graphene sheet is reduced and the Brillouin zone folds into a mini Brillouin zone.

Version of November 25, 2018– Created November 25, 2018 - 02:09

Depending on the twist angle, the periodicity of the Moiré pattern changes, and with it, the strength of the interlayer coupling. It was found that for large twist angles ($\theta > 15°$), the interlayer hybridization is minor and the band structure can be evaluated as a single graphene sheet including a small perturbing potential (ignoring certain commensurate rotation angles where full two-dimensional periodicity is restored).

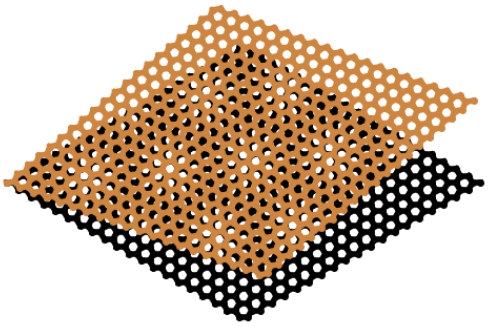

Figure 2.2: *Illustration of a Moiré pattern created by stacking two honeycomb lattices with a relative twist angle of* $\theta = 10°$.

However, for general small twist angles ($\theta < 10°$), interlayer effects become very strong and a different theoretical treatment is required to describe the electronic properties of the bilayer.

A full theoretical treatment of the small twist angle regime is presented in the work of Bistritzer and MacDonald [7]. They present a low-energy continuum Hamiltonian that captures both the intralayer and interlayer hopping as a function of the twist angle between them. In this new model, the band structure of the bilayer is described by so called Moiré Bloch bands. Bistritzer and MacDonald show that the Dirac cones at the K and K′ points mix due to interlayer interactions. Most of the electronic states are contained in AA stacked areas of the superlattice, although some are present in AB stacked zones. More astonishing though, is the observation the flattening of the lowest of the Moiré Bloch bands, observed for a specific set of angles. At these "magic angles", the Fermi velocity at the Dirac point becomes 0. This is very interesting, since flat bands translate to a very high density of states (DOS), and therefore give rise to a strong intraband electron-electron correlation. In combination with a small bandwidth, this can result in strong localization of the electronic states, and all kinds of other correlated electronic phases.

Mottness in MA-TBG

The relevance of this theoretical work was emphasized very recently, when Cao *et al.* [1, 2] presented transport data on samples of MA-TBG. They measured TBG samples with a twist angle of $\theta = 1.05°$ and $\theta = 1.16°$ respectively, very close to the theoretically predicted magic angle of $\theta = 1.1°$.

Version of November 25, 2018– Created November 25, 2018 - 02:09

To electronically isolate the graphene bilayer from its environment, the bilayer is sandwiched between hexagonal Boron Nitride (hBN), and then placed on top of a metal gate in order to control the carrier density inside the bilayer. Due to its large band gap, hBN only interacts very weakly with the graphene. By choosing a relatively large stacking angle between the hBN sheet and the graphene, their coupling is only minimal. Therefore, hBN is an excellent material to isolate the bilayer.

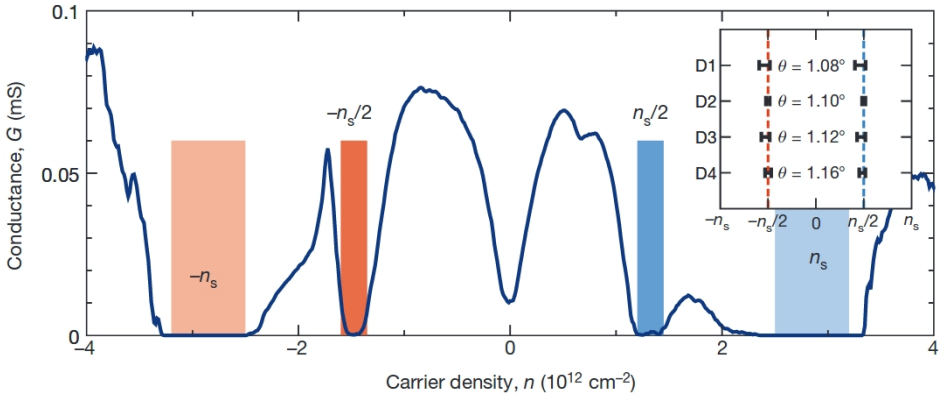

Figure 2.3: *Resistivity measurements as a function of doping for a MA-TBG sample with a twist angle of $\theta = 1.05°$, measured at T = 0.3K. The lighter shaded regions correspond to superlattice gaps induced by the Moiré structure at carrier density of $\pm n_s \approx 2.5 \times 10^{12} cm^{-2}$. The gaps indicated by the darker shaded regions at half the carrier density of the superlattice gaps, however, do not appear in the single particle DOS. The inset shows the dependence of n_s on the relative twist angle. Image from reference [1].*

Resistivity data for different carrier densities measured at 0.3K is presented in figure 2.3. At a carrier density of $\pm n_s \approx 2.5 \times 10^{12} cm^{-2}$, the data shows an insulating gap that corresponds to the gap induced by the superlattice modulation of the Moiré pattern. The gap observed at half of this carrier density ($\pm \frac{n_s}{2}$), however, cannot be explained by the tight-binding results of Bistritzer and MacDonald [7], and therefore seems to be a many-body effect. More specifically, because this insulating state occurs at exactly half filling of the lowest of the Moiré bands (2 electrons per unit cell), this strongly hints at the emergence of a Mott insulating state at this carrier density, which will be explained in box 1.

Version of November 25, 2018– Created November 25, 2018 - 02:09

Box 1: Mott insulators

A Mott insulator is one of many electronic phases found in strongly correlated materials, formed when the intraband Coulomb energy exceeds its bandwidth. Such a system can be described by the Hubbard model:

$$H = \sum_{i,j,\alpha,\beta} t_{ij,\alpha\beta}\, c^{\dagger}_{i,\alpha} c_{j,\beta} + h.c. + U \sum_{i,\alpha} n_{i,\alpha}(n_{i,\alpha} - 1) \tag{2.2}$$

In this equation, $c_{i,\alpha}$ is the annihilation operator for a particle at site i in orbital α, and $n_{i\alpha}$ is the corresponding occupation number operator. t and U are the hopping amplitude and the Hubbard (electron-electron) repulsion respectively. Balancing these parameters results in different electronic phases: When the Hubbard repulsion is much stronger than the hopping parameter, which is proportional to the electronic bandwidth of the material ($W \sim t$), the electronic states become highly localized and the model describes a Mott insulator (figure 2.4). On the other hand, when $U/t \ll 1$, the model describes a (semi-)metallic system with some correlations.

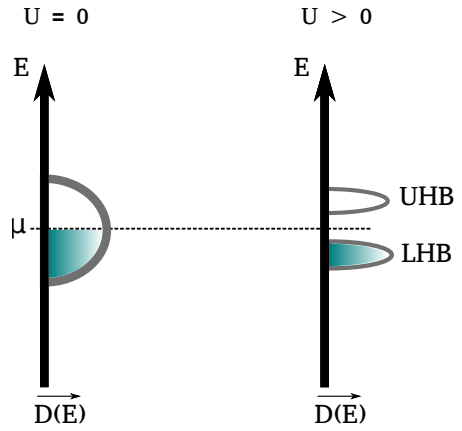

Figure 2.4: *In a Mott insulator, due to strong electron-electron interactions, the conduction band splits in an upper- and lower Hubbard band. As a result, the material is insulating at half filling.*

In materials with substantial electron-electron correlations, like the famous copper oxides, electronic states can become localized, in accordance with the model above. Electron transport can only take place if

Version of November 25, 2018– Created November 25, 2018 - 02:09

an electron hops from one site to another, which requires a characteristic energy U that originates from the Coulomb interaction. In other words, instead of a steady flow of electrons, transport in these material closely resembles a bunch of people trying to cross a river over a path of stepping stones. The insulating state that occurs as a result of this effect is called a Mott insulator. In the past years, it has been confirmed that high-T_c superconducting phases appear when we dope a Mott insulator [8, 9]. In iron-based superconductors, it is still uncertain how Mott-like behavior gives rise to the observed unconventional superconductivity, because the parent compound is actually a metallic ferromagnet as opposed to an insulating antiferromagnet in the case of cuprates. Currently, it is believed that the iron-based compounds exhibit a so called orbital selective Mott state [10]. As the name suggests, this entails that only certain orbitals form bands through which carriers are transported, whereas others form a Mott state: The iron-based superconductors are thought to have a Mott state which is concealed by their metallic behavior, i.e. correlated- and uncorrelated electrons coexist in these materials.

A new platform to study unconventional superconductivity

Mott insulators are especially interesting since in the past few years, it has been established that high-T_c superconductivity arises from doping a Mott state [8, 9]. In MA-TBG, the realization of a Mott state is possible due to the flatness of the lowest Moiré band and the large DOS associated with it. In reference [2], Cao *et al.* actually showed that superconducting domes appear in the phase diagram of the MA-TBG samples when doping away from the insulating state, closely resembling that of cuprates (figure 2.5a, 2.5b).

The sample with $\theta = 1.05^\circ$, which exhibits a metal to (Mott)insulator transition at 4K, shows superconductivity when the back gate voltage was shifted away from the Mott state, with a maximum measured T_c of 1.7K. At first glance, this seems rather disappointing when compared to the record high T_cs achieved in for example BSCCO (T_c = 108K) or monolayer FeSe on STO ($T_c \sim$ 65K). It should be pointed out though, that the carrier density at which superconductivity occurs in TBG is much lower than that of other high-T_c superconducting compounds. In this context, a T_c of 1.7K is actually very large, suggesting an even stronger pairing mechanism than that observed in the cuprates.

In figure 2.5c, the four-probe resistivity data of Cao *et al.* [2] is displayed. Figure 2.5a contains a stripped-down version of the cuprate phase diagram, a full version of which is displayed in figure 2.5b. We know of a rich variety of phases that appear in the diagram of the cuprates. MA-TBG was only recently discovered as an unconventional superconductor, and because it has only been studied in transport experiments so far, it is currently not possible to describe its phase diagram in more detail. However, because of the Mott state that is present in the current phase diagram, and the additional analogy with cuprates, we deem it highly likely that MA-TBG will have a much more elaborate phase diagram with respect to what is revealed thus far. For this reason, we would like to further investigate the phase diagram of MA-TBG by studying it with an STM. Based on its previous successes in studying cuprates and iron-based superconductors, we think STM is an excellent technique to study MA-TBG as well. In this thesis, we carry out some of the necessary preparations in order to do so, mainly focusing on the aspect of landing on micrometer-sized graphene flakes, and tip induced band banding (TIBB), an effect expected to occur in graphene due to the relatively low carrier densities present in the material.

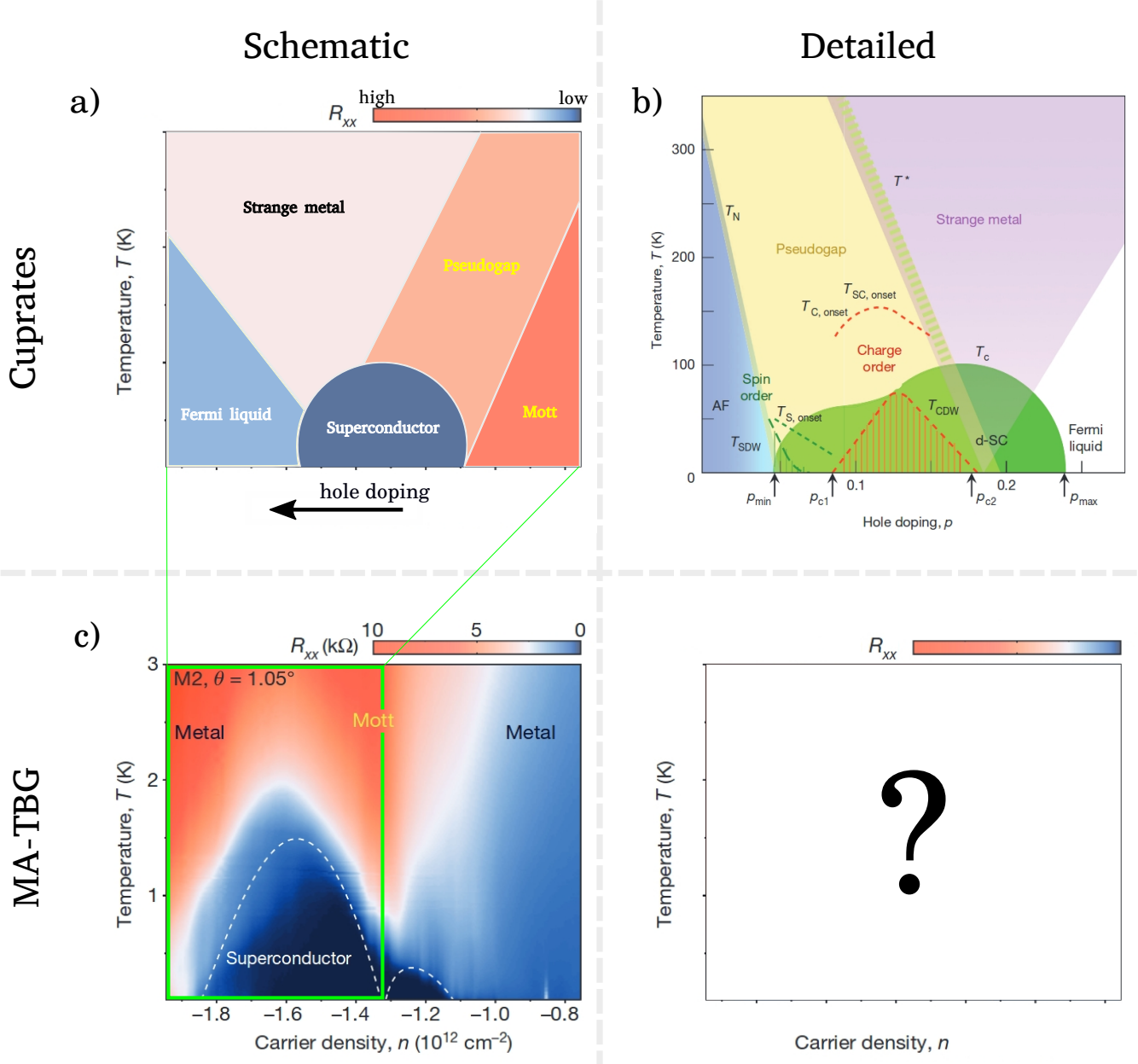

Figure 2.5: *a) Schematic phase diagram of the cuprates. b) Detailed phase diagram of the cuprates. Image taken from reference [8]. c) Four-probe resistivity measurements of MA-TBG ($\theta = 1.05°$) as a function of temperature and doping. Image from reference [2]. The transport data shows remarkable similarities to the cuprate phase diagram.*

Chapter 3

Scanning Tunneling Microscopy

Ever since its invention in the 17th century, the optical microscope has allowed humans to study objects with extremely small dimensions. The instrument is made up out of a collection of lenses that manipulate the lightrays from the object. Unfortunately, because of the diffraction limit, these instruments cannot image objects that are smaller than several µm, half of the wavelength of visible light. To overcome this, electron based microscopes were invented.
A Scanning Tunneling Microscope, or STM, is an electron microscope based on the quantum mechanical effect of tunneling: Where classical theory does not allow particles to cross a potential barrier when their energy is lower than said barrier, due to the particle-wave duality in quantum theory, a particle incident on a potential barrier can have a finite probability to end up on the other side of it. This effect is called tunneling.
Typically, the founding work of STM is considered to be done by Binnig and Rohrer in 1983 [11]. What is often not mentioned however, is a paper published in 1972 already, by Young, Ward and Scire on an instrument called the topographiner [12]. Their instrument was based on having a small emitter ($\sim 100 - 10000$ Å) (cathode) close to the to be imaged surface (anode) in a vacuum. When passing a constant current through the emitter, a constant electric field originates from it, creating a finite potential between the emitter and surface, which depends on the distance between them. This voltage is measured an coupled back to a servo system made from piezoelectric elements, in order to keep the emitter at a constant height above the surface. Then, by moving emitter laterally with respect to the surface, its topography can be deduced.
The only problem with this technique was its resolution: using typical emitters at the time (~ 10 Å), the best resolution achievable would be the-

oretically be limited to 100 Å. Binnig and Rohrer built a device similar to this, however, instead of relying on field emission, the topography is inferred by measuring a tunneling current. Instead of using an emitter, the STM is based on an atomically sharp tip which is brought close to a surface (several Å). The vacuum gap between the tip and surface behaves as a potential barrier for electrons. As mentioned above, from quantum theory, we know that it is possible for particles to tunnel through a barrier, in this case, from tip to sample or vice versa. Because of the symmetry of the tunnel junction, the probability to tunnel in the former case equals that of the latter. Therefore, there will be no net current. In order to overcome this, a finite bias voltage is applied between the tip and sample, favoring one of the two tunnel processes thereby generating a finite current.

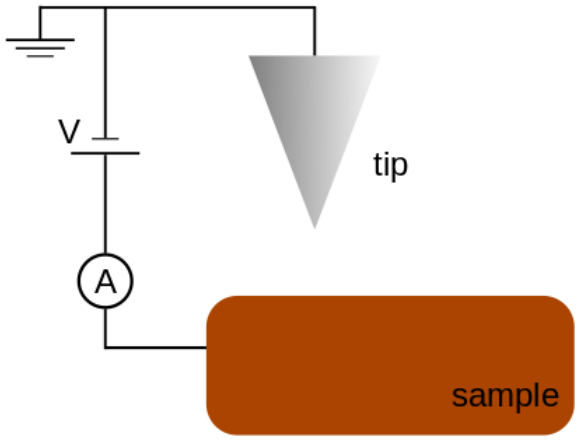

Figure 3.1: *Schematic overview of a scanning tunneling microscopy setup. An atomically sharp tip is moving parallel to the surface, measuring the tunneling current at each location. In this way, the electronic properties of a sample can be determined with atomic precision.*

Importantly, this tunneling current scales exponentially with the width of the tunnel barrier, *i.e.*, the distance between the tip and sample. This is easy to see by just calculating the probability ($|\Psi|^2$) of an electron to appear on the other side of an infinitely large potential barrier from the

(time-independent) Schrödinger equation:

$$\begin{aligned} H\Psi &= E\Psi \\ -\frac{\hbar^2}{2m}\frac{\partial^2\Psi}{\partial x^2} + V\Psi &= E\Psi \\ \text{Plane wave ansatz} : \Psi &\sim e^{kx} \\ -\frac{\hbar^2 k^2}{2m} &= (E-V)\Psi \\ k &= \pm i\frac{\sqrt{2m(E-V)}}{\hbar} \end{aligned}$$

Notice how when the electron has an energy higher than the potential (outside the barrier, $E > V$), k is fully imaginary and the electron wave function is just a plane-wave. In the potential barrier itself, however, $E < V$ and k becomes real. In order for the wave function to not diverge, only $k < 0$ can be a valid solution and we see that the wave function decays exponentially inside the tunnel barrier. This is a key mechanism behind the excellent vertical and lateral resolution of STM: only a small difference in tip-sample distance ($\sim$ Å) can substantially change the tunneling current.
A more in-depth theoretical understanding of quantum tunneling is provided by Bardeen [13]. Later, Tersoff and Hamann [14, 15] applied this to STM. Using Fermi's golden rule, they showed that the tunneling current obeys:

$$I = \frac{2\pi e}{\hbar}\sum_{\mu\nu} f(E_\mu)[1 - f(E_\nu + eV)] \times |M_{\mu\nu}|^2 \delta(E_\mu - E_\nu) \tag{3.1}$$

In this expression, $f(E_i)$ is the Fermi distribution function, V is the bias voltage and $|M_{\mu\nu}|^2$ is the matrix tunneling element, which can be calculated according to Bardeen as [13]:

$$\begin{aligned} M_{\mu\nu} &= -\frac{\hbar^2}{2m}\int d\mathbf{S}\cdot(\Psi_\mu^*\nabla\Psi_\nu - \Psi_\nu\nabla\Psi_\mu^*) \\ &= -\frac{\hbar^2}{2m}\int d\mathbf{S}\cdot\mathbf{J}_{\mu\nu} \end{aligned} \tag{3.2}$$

The integral is performed over the entire surface lying in the vacuum gap between the tip and sample.
In order to evaluate $M_{\mu\nu}$, Tersoff and Hamann assumed a general form for the sample wavefunctions (plane-waves). Furthermore, since the tip states

Version of November 25, 2018– Created November 25, 2018 - 02:09

and tip geometry are generally unknown as well, they assumed an s-like wave function for the tip and a spherical geometry, as displayed in figure 43. Using this, and assuming the low temperature and low bias limit, they found that:

$$I \sim V n_t(E_f) e^{2\kappa R} \sum_{\nu} |\Psi_\nu(\mathbf{r_0})|^2 \delta(E_\nu - E_f) \tag{3.3}$$

Here, $n_t(E_f)$ is the density of states of the tip at the Fermi level, $\kappa = \hbar^{-1}\sqrt{2m\phi}$, is the inverse of the decay length of the wave function and ϕ is the work function. The summed over expression is regarded as the local density of states of the sample: LDOS $= \sum_{\nu} |\Psi_\nu(\mathbf{r_0})|^2 \delta(E_\nu - E_f)$.

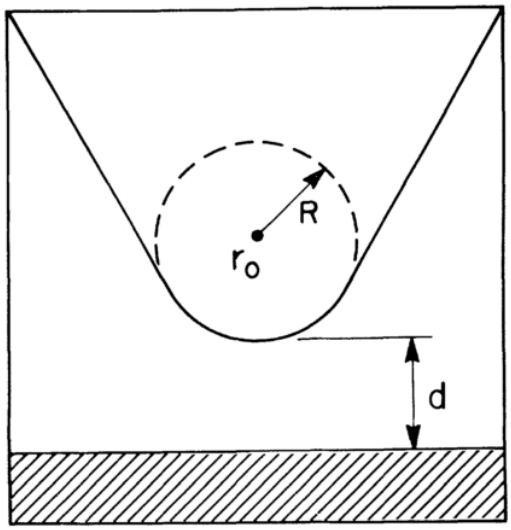

Figure 3.2: *Tip geometry assumed by Tersoff and Hamann. In their paper,* $\mathbf{r_0}$ *indicates the center of curvature of the tip. The radius of curvature is given by R and the distance on nearest approach is given by d.*

As we can see from equation 3.3, the tunneling current depends on the LDOS of the sample. More specifically, the differential conductance, $\frac{dI}{dV}$, is directly proportional to it. This is utilized in a technique called scanning tunneling spectroscopy. An AC bias is superimposed on the regular DC bias, with a frequency higher than the bandwidth of the feedback electronics. Using lock-in technique, the in-phase component is measured, yielding $\frac{dI}{dV}$. The carrier frequency is chosen higher than the cutoff frequency of the electronics in order to prevent the the feedback from compensating for it. The amplitude of the modulation should be chosen small enough in order to resolve the spectral features of the LDOS. Additionally, the measured features are affected by thermal broadening ($5.4k_bT$). Therefore, this

measurement technique can only be applied in a low temperature environment.

Chapter 4

STM on micrometer-sized flakes: Capacitive navigation

Exfoliated graphene flakes usually have a surface area on the order of several μm^2. This makes them a tricky candidate for studies involving STM: It is rather difficult to land with the tip on a patch of these dimensions. Some setups allow for optical acces to the scanner, which makes it easier to align the flake with the tip. Unfortunately, not every setup has optical access, because of the need of for example ultra low temperatures.
To overcome this obstacle in a setup without optical access, some research groups choose to stamp their flake on a sample containing pre-patterned macroscopical contacts [16, 17]. By scanning such samples and extracting the information from the topological features patterned on the sample, the tip can be navigated towards the flake. The downside of this method, however, is that finding the flake is a rather slow process. This has to do with the intrinsic limitations of STM: To achieve atomic resolution on the regular, the working principle of an STM setup relies on a piezoelectric scanning tube. The length of this tube, together with its diameter determine the maximum field of view of the microscope. In designing the microscope, choosing the dimensions of the tube scanner is equivalent to balancing the maximum field of view versus mechanical noise [18]. As a result of this, typical microscopes have a maximum XY-range of about $\lesssim$ 10 µm at low temperatures.
To extend the XY-range, most microscopes rely on a separate XY-stage to accurately move the sample over larger distances, extending the effective field of view. Then, finding a graphene flake by following topological features on the sample entails taking many topographs in different locations and combining their information to eventually navigate to the flake, a very

time consuming process.
Alternatively, the work of Andrei *et al.* [19] shows that it is possible to find the microscopically small flake by capacitively scanning the contour of the sample under study. This method, other than relying on the presence of a backgate in the sample under study, requires no additional components except for a standard STM setup.
The technique relies on measuring an AC component in the tunneling current. During normal operation, the microscope measures the DC tunneling current which flows between tip and sample. From what nowadays is considered routine Scanning Tunneling Spectroscopy (STS) measurements, we know that it is also possible to measure AC components of the tunneling current. The total current measured by the microscope is given by:

$$I = \frac{V_{bias}}{|Z_j|} \tag{4.1}$$

In this expression, V_{bias} is the applied bias voltage (the potential difference between tip and sample), and Z_j is the complex impedance of the tunnel junction. Generally, we can model the impedance of the junction as a parallel resistor-capacitor circuit. The bias contains the normally applied DC bias (V), in addition to a small AC modulation ($\tilde{V}$). This means that the tunnel current can be written as:

$$I = G_t V + G_t \tilde{V} + i\omega C\tilde{V} = G_t V_{bias} + i\omega C\tilde{V} \tag{4.2}$$

Here, G_t is the junction conductance, C is the tip-sample capacitance, and ω is the frequency of the applied modulation signal.
When the tip is relatively far away from the sample, G_t is infinitesimally small, and no DC current can be measured. However, due to the finite capacitance between the probe tip and the sample, it is possible to measure the AC signal. Furthermore, because the capacitance (C) is spatially dependent, it is possible to map out the contours of the sample by measuring the AC component of the current. According to reference [19], for typical scanning parameters ($\tilde{V}$ = 200 $\mathrm{mV_{rms}}$ at 5 kHz), the AC current can be detected several mm away form the sample.
The fact that the capacitance is spatially dependent finally allows the microscope to map out the contours of the sample just by measuring the AC component of the current. Figure 4.1 demonstrates this, and the purpose of the backgate.

Version of November 25, 2018– Created November 25, 2018 - 02:09

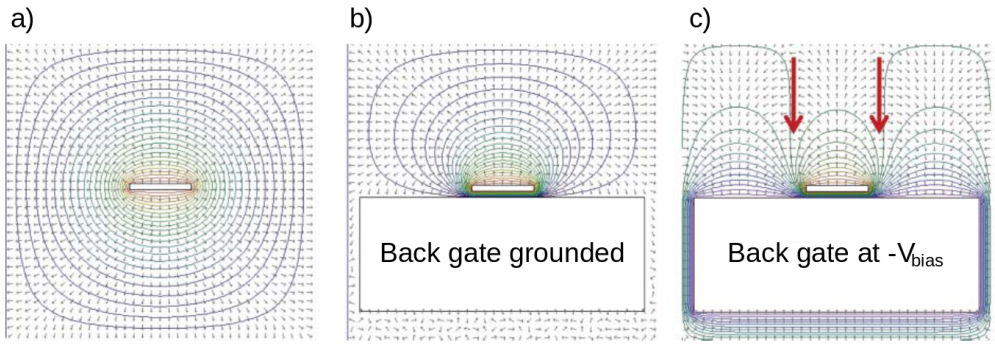

Figure 4.1: *Equipotential lines of the electric field for:* ***a)****, a biased, conducting sample* ***b)****, a biased, conducting smaple in the presence of a grounded backgate* ***c)****, a biased, conducting smaple in the presence of a backgate, where the gate voltage is chosen equal in magnitude to the bias, but 180° out of phase. Image taken from reference [19].*

Normally, when the bias voltage is applied to the conductive contacts, the equipotential lines of the electric field quickly lose the shape of the contacts (figure 4.1a). Putting a grounded, metallic plate below the contacts, however, drastically increases the distance over which the electric field retains the shape of the contact (figure 4.1b). Finally, by applying an equal but opposite bias voltage (180° out of phase) to the backgate, sharp features appear in the electric field at the edges of the contact (figure 4.1c). These features decay over a distance which is proportional to the size of the contact. According to reference [19], to accurately resolve the size of the contact, an aspect ratio ≤ 0.3 is requires, where the aspect ratio is defined as $\frac{\text{tip sample distance}}{\text{feature size}}$.
One can use this capacitive trick to navigate towards, for example, a micrometer-sized graphene flake. To this purpose, the authors of reference [19] suggest a sample as displayed in figure 4.2.

Version of November 25, 2018– Created November 25, 2018 - 02:09

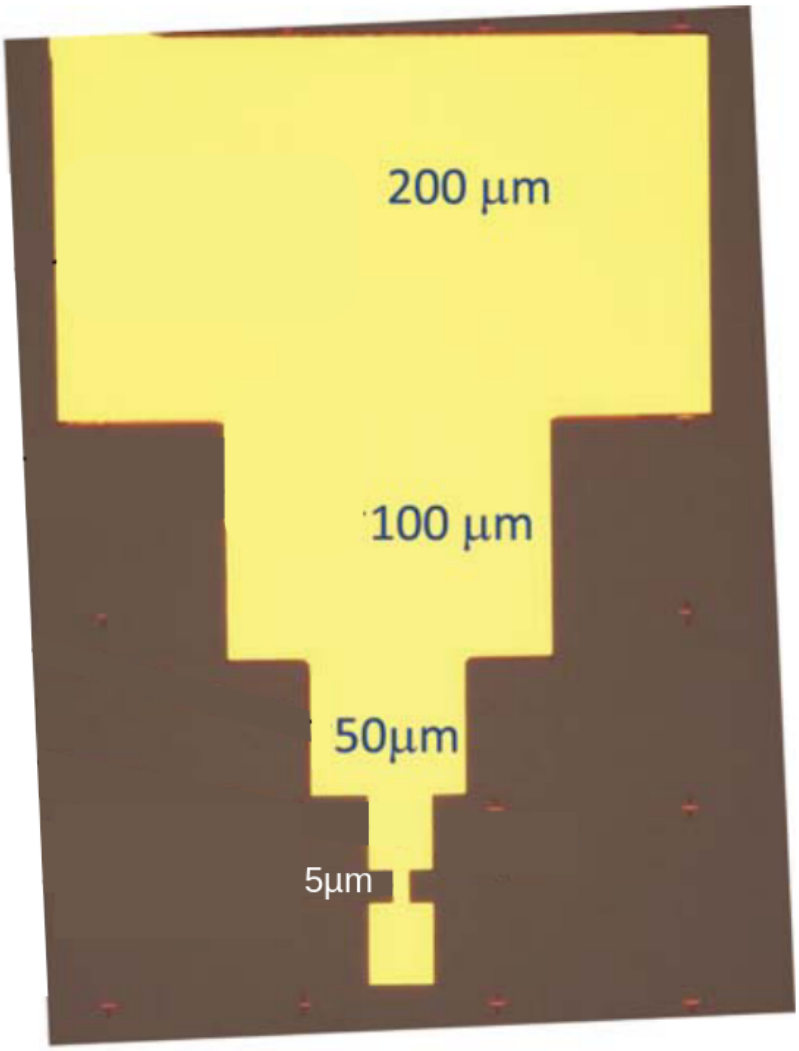

Figure 4.2: *Optical image of the sample used in reference [19]. The actual width of each feature is written in the image. Image taken from reference [19].*

Gold contacts are patterned on top of a doped Si/SiO_2 wafer. The doped Si acts as a backgate. By patterning the contacts in this way, the graphene flake is intended to be stamped at the apex of the smallest feature of the contact. By arranging the chip position as to center the biggest pad roughly in the middle of the sampleholder, one maximizes the chance of landing with the tip on the biggest contact pad. Then, by capacitively mapping out the contour of the whole contact, one can navigate towards the flake.

In this work, we design a testsample for testing capacitive navigation in our STM setup. Unfortunately, because the setup was defective at the time of this project, we could not do the actual test.

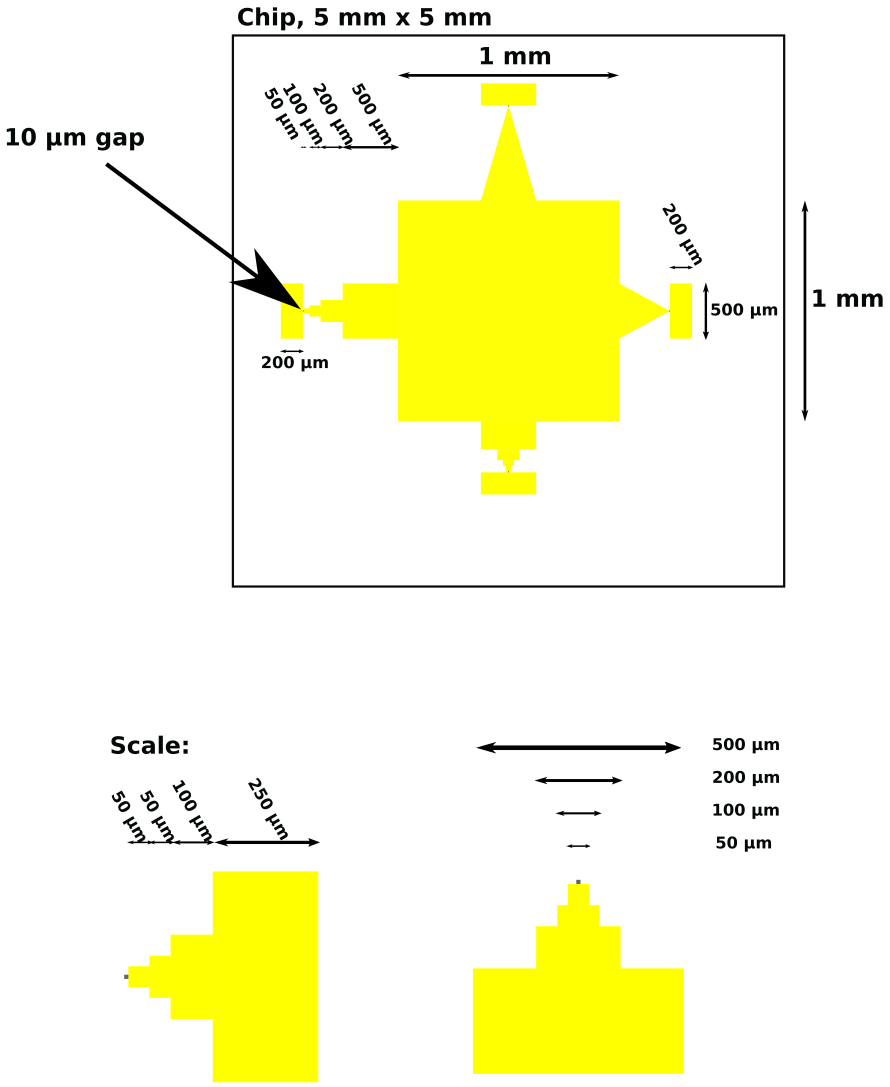

Figure 4.3: *Schematic of the sample we designed for capacitive nagigation in our system. In practice, a graphene flake can be placed in one of the four 10 µm gaps pointed out by the arrow.*

We create a large platinum contact on a Si/SiN chip using standard optical lithography. The design for the contact is displayed in figure 4.3. In practice, the graphene flake will be positioned at one of the four small pads, which in our case is 50 µm x 50 µm. Instead of gold, we choose to make our contacts out of platinum, keeping in mind the future use for these devices: the study of graphene flakes. Since platinum acts as a catalyst for removing polymer residues when annealing the graphene [20], it seems beneficial to use platinum instead of gold electrodes.
We decided to make four different branches on the testsample, in order to test which design gives the fastest and most reliable tip navigation.

4.1 Testsample fabrication

To create the contact, we spin-coat a chip with AZ5214 optical resist (4000 rpm, thickness = 1.4 µm). After that, we use a laserwriter (DMO ML-2) to transfer our design into the resist. We expose with a laser (spotsize 1 µm) having a wavelength of 405 nm, using a dose of 400 mJ/cm^2. After writing, we develop the chip in a 1:3.5 solution of AZ400 and water (H_2O). This takes approximately 10 s. We stop the development process by rinsing the chip with water.
Then, we sputter approximately 50 nm Pt and perform lift-off in acetone. When necessary, we sonicated the chip for 2 seconds in order to remove the resist. The sputtering is done using a Leybold Z400 sputtering machine. Later inspection of the chip using a profilometer (KLA/Tencor D-120) revealed that the actual thickness of the platinum layer is approximately 51 nm (figure 4.4). The final result is displayed in figure 4.6.

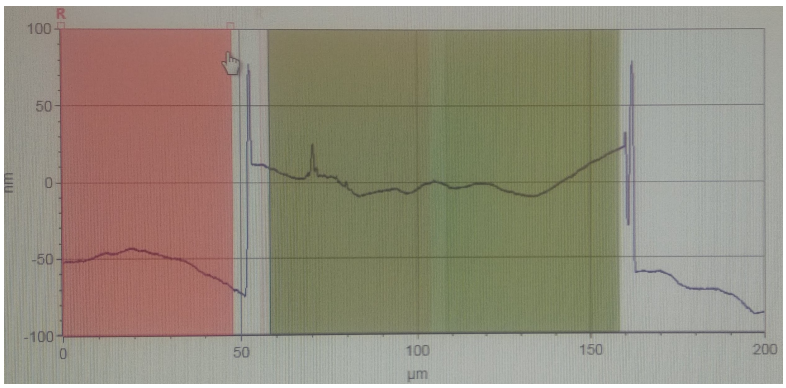

Figure 4.4: *Photograph of the profilometer display, after tracing over one of the branches after lift-off. The green contour indicates the platinum contact. We estimate the thickness of the Pt film to be approximately 51 nm.*

After fabrication, we inspected the chip with an optical microscope. An image of part of the chip is included in figure 4.5

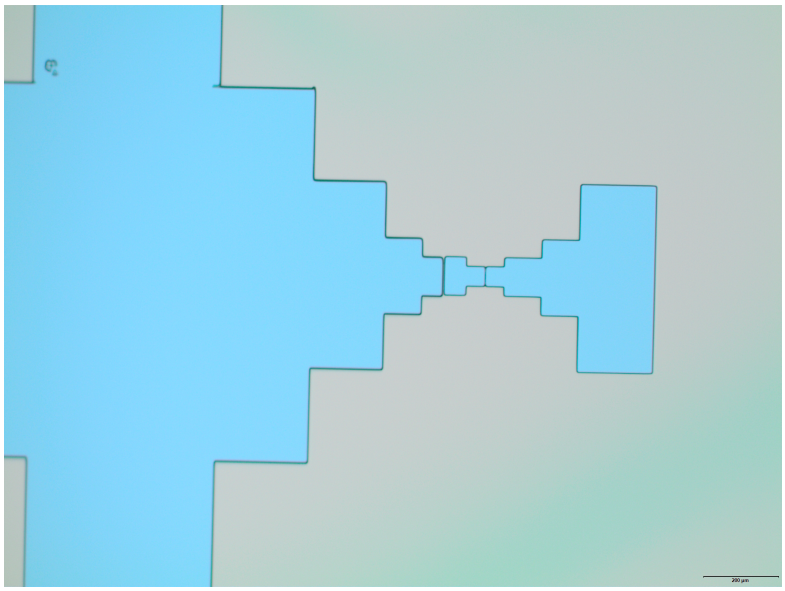

Figure 4.5: *Optical image of part of one of our fabricated testsamples. Unfortunately, some samples show a trench through the pad. We believe this is an artifact from the laserwriter.*

Unfortunately, some samples show a trench in the pads. We believe this is an artifact of the laserwriter we used to expose the resist. This phenomenon occurs when the turbo mode is enabled, resulting in rendering errors of the pattern in the control software.

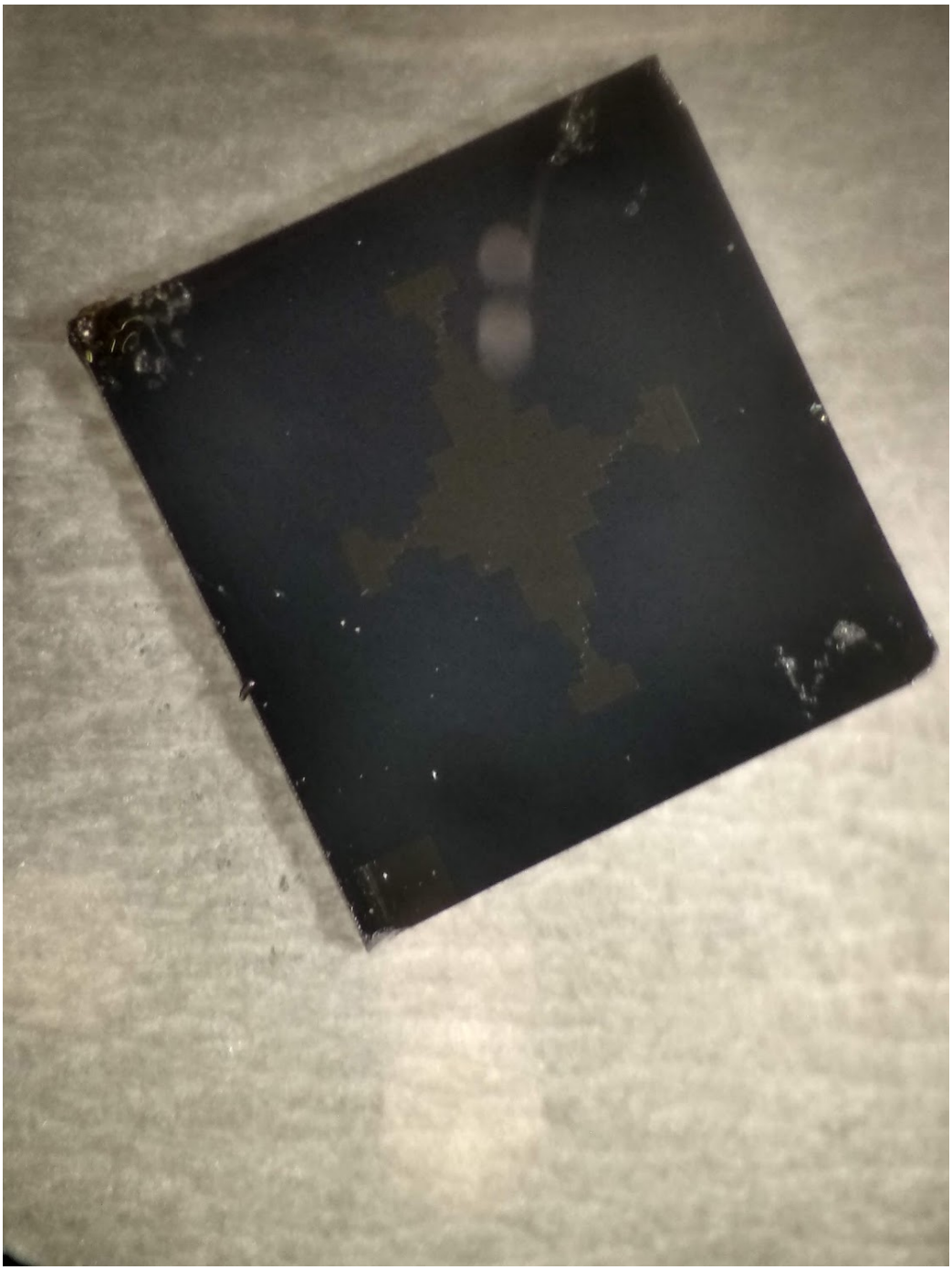

Figure 4.6: *Picture of one of our fabricated testsamples.*

Chapter 5

Tip Induced Band Bending in graphene samples

As discussed in chapter 2, graphene has a relatively low carrier density. This is quite a favorable property in most cases, because it allows for tuning of the chemical potential using standard electrostatic doping. To this purpose, in most studies, it is common to use a doped Si wafer as a chip substrate and utilize it as a backgate [17, 19, 21].
Unfortunately, there is also a downside to this property with regards to studying it with STM. In chapter 3, we discussed the working principle of a conventional STM. To briefly recap: an STM measures the tunneling current between a probe tip and the sample under study. To realize a finite tunneling current, a bias is applied between the tip and sample. This means that during normal STM operation, a metal electrode with a different electric potential is in close proximity (~ 5 Å) to the sample under study. In most cases, this scenario has no further implications since most samples studied with STM are metallic. Due to the high free carrier densities in these materials, the electric field emitted by the tip is effectively screened, and therefore, of no further consequence. In graphene, however, this is no longer the case due to the presence of relatively few free carriers. A similar situation occurs when studying semiconductors with STM. In this field of research, a commonly known phenomenon that manifests itself as a result of this is Tip Induced Band Bending (TIBB) [22–24].
Because the tip- sample junction is biased, the tip has a finite potential difference with respect to the sample. As a result of this, an electric field emanates from the tip or sample, depending on the sign of the potential difference. Because only few free carriers are present in the graphene, this electric field is not fully screened, and hence it will attract/repel free car-

riers in the graphene sheet. The phenomenon described here is actually the same mechanism at work when it comes to electrostatic doping: TIBB is nothing more than the effect of locally gating the sample with the probe tip.
In the MA-TBG system, this effect can be very unfortunate since the periodicity associated with the Moiré lattice is quite long ($\sim$ 15 nm). Because the tip acts as a nanoscale gate, we fear that the TIBB effect will destroy this periodicity, thereby possibly impairing the observed phenomena in this system. It is thus far unclear how severe the effect of TIBB is on MA-TBG.
In this work, we try to predict the effect of having a probe tip in close proximity to a system of bilayer graphene. We do this following the model presented by Min *et al.* [25]. Here, the carrier distribution of few-layer graphene grown by thermal decomposition of silicon carbide (SiC) is calculated. We apply this model a system of bilayer graphene deposited on hBN, carefully pointing out the weaknesses, and the major differences of this model with respect to the work presented in reference [25].

5.1 Charge distribution few-layer graphene

Following the work of reference [25], we model M individual layers of graphene deposited on a certain substrate (see figure 5.1). In equilibrium, all layers share the same chemical potential, μ. The energy spectrum of each layer is given by the energy spectrum of a single graphene layer, shifted by the local potential, u_i. This implies that the charge density of layer i, is given by:

$$\sigma_i = \frac{\mathrm{sgn}(\mu - u_i)}{\pi} \left(\frac{\mu - u_i}{\hbar v} \right)^2 \tag{5.1}$$

In this expression, $\hbar$ is the reduced constant of Planck, and v is the carrier velocity of the π-band at the dirac point. The latter is proportional to the intralayer hopping amplitude, γ_0, and can be calculated according to:

$$v = \frac{\sqrt{3}a}{2} \frac{\gamma_0}{\hbar} \tag{5.2}$$

Here, a is the lattice constant of graphene (a = 2.46 Å), and γ_0 is taken to be 3 eV (reference [25]). This gives of a carrier velocity of 9.71×10^5 m/s.

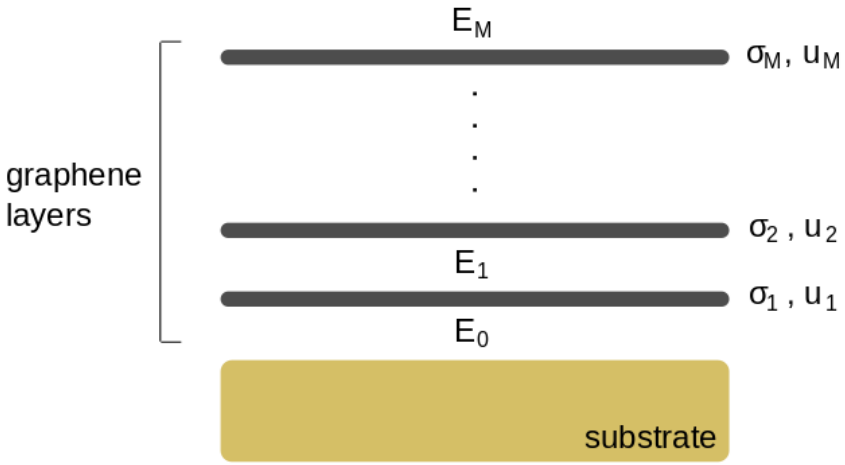

Figure 5.1: *Overview of the few-layer graphene model used in this section. Each graphene layer is characterized by its own charge density and the local potential, σ_i and u_i respectively. The electric field between layer i and i+1 is given by E_i.*

We calculate the local potential from the charge densities using the Poisson equation. The electric field between layer i and i+1, E_i, statisfies:

$$E_i - E_{i-1} = (-e)\,\frac{\sigma_i}{\epsilon_0}, \tag{5.3}$$

where ϵ_0 is the vacuum permittivity. Finally, the local potential can be obtained by iterating:

$$u_{i+1} = u_i + edE_i \tag{5.4}$$

Here, d is the interlayer distance in graphene, d = 0.335 nm (reference [25]). A boundary condition is created by the substrate. This fixes the value of $u_1 - \mu$, and can experimentally be determined with spectroscopic measurements [26]. For few-layer graphene on SiC, the authors of reference [25] choose $u_1 - \mu$ = 360 meV, in accordance with the work presented in reference [26]. On hBN, we expect this number to be much smaller. The reason for this is the relatively large free carrier count present in the buffer layer which eventually sits between the few-layer graphene and the SiC substrate. Obviously, this layer is absent when stamping graphene on hBN. Since we mainly consider bilayer systems on hBN, in this work, we therefore choose $u_1 - \mu$ = 50 meV.

5.2 Charge distribution in bilayer graphene

We start by considering a bilayer system (M = 2) without the presence of a probe tip. In this situation, we can assume that the electric field outside the bilayer vanishes, *i.e.* $E_2 = 0$. Using equation 5.3, we obtain an expression for E_1, the electric field between the layers:

$$E_1 = e\,\frac{\sigma_2}{\epsilon_0} \tag{5.5}$$

Furthermore, we choose our zero energy such that $u_1 = 0$. According to equation 5.4, this means that u_2 is given by:

$$u_2 = edE_1 = \frac{e^2 d}{\epsilon_0}\sigma_2 \tag{5.6}$$

Additionally, equation 5.1 implies that:

$$\sigma_1 = \frac{1}{\pi}\left(\frac{\mu}{\hbar v}\right)^2, \tag{5.7}$$

$$\sigma_2 = \frac{\mathrm{sgn}(\mu - u_2)}{\pi}\left(\frac{\mu - u_2}{\hbar v}\right)^2 \tag{5.8}$$

Using equation 5.6 and 5.8, we numerically solve for u_2. Finally, we use this result to calculate σ_2 using either equation 5.6 or 5.8. We find that $\frac{\sigma_2}{\sigma_1} \approx 0.53$. This implies that the charge distribution over the two graphene sheets is already significantly anisotropic to begin with.

5.3 Charge distribution in bilayer graphene in the presence of a probe tip

To calculate the charge distribution in a system of bilayer graphene in the presence of a probe tip, we repeat the procedure described in the previous section. The probe tip is modeled as an extra plate above the bilayer, separated by a distance equal to d_{ts}. As a result of this, $E_2 \neq 0$.

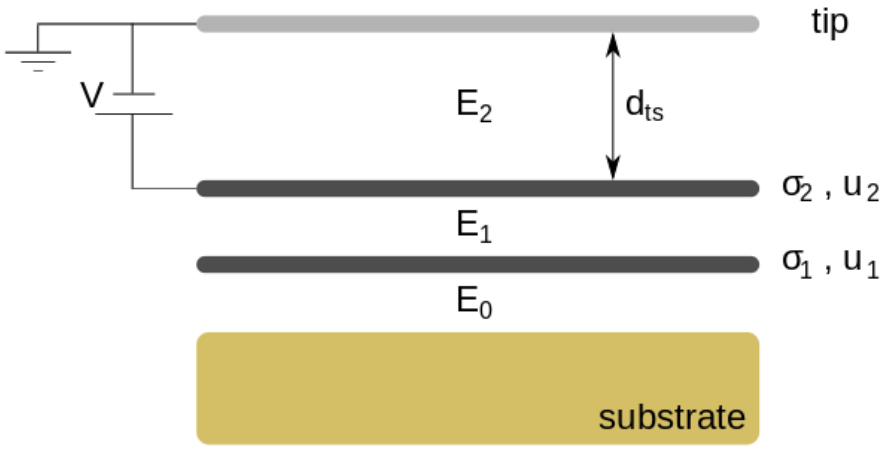

Figure 5.2: *Overview of the few-layer graphene model used in this section. Each graphene layer is characterized by its own charge density and the local potential, σ_i and u_i respectively. The electric field between layer i and i+1 is given by E_i. The tip is modeled as an extra plate, a distance d_{ts} above the sample. As is convention in STM, the bias is applied to the sample.*

We can determine the value of E_2 by realizing that the chemical potential of the tip is given by:

$$\mu^{tip} = \mu + eV = u_2 + \Phi + ed_{ts}E_2 \tag{5.9}$$

In this expression, V is the bias voltage between the tip and sample, and $\Phi = \Phi_{graphene} - \Phi_{tip}$, is the difference between the work function of graphene and the tip. According to reference [21], the work function of graphene is given by $\Phi_{graphene} \approx 4.6$ eV. For a PtIr tip, $\Phi_{PtIr} \approx 5.2$ eV (reference [21]). Rewriting 5.9, we get:

$$E_2 = \frac{\mu + eV - \Phi - u_2}{ed_{ts}} \tag{5.10}$$

Using equation 5.3, we again obtain an expression for the electric field between the two graphene sheets:

$$E_1 = E_2 + e\frac{\sigma_2}{\epsilon_0} = \frac{\mu + eV - \Phi - u_2}{ed_{ts}} + e\frac{\sigma_2}{\epsilon_0} \tag{5.11}$$

Then, using equation 5.4, we obtain a relation between u_2 and σ_2:

$$u_2 = u_1 + edE_1 = ed\left(\frac{\mu + eV - \Phi - u_2}{ed_{ts}} + e\frac{\sigma_2}{\epsilon_0}\right) \tag{5.12}$$

Note that we again choose our zero energy such that $u_1 = 0$. Rewriting in terms of σ_2, we find:

$$\sigma_2 = \frac{\epsilon_0}{e^2}\left(\frac{u_2}{d} - \frac{\mu + eV - \Phi - u_2}{d_{ts}}\right) \tag{5.13}$$

Finally, we can combine equation 5.13 and 5.8, and solve for u_2, σ_2. In figure 5.3,5.4, we do this for different tip- sample distances (d_{ts}) and different bias voltages (V). We plot the ratio $\frac{\sigma_2}{\sigma_1}$, as function of the applied bias voltage (V), and tip- sample distance (d_{ts}).

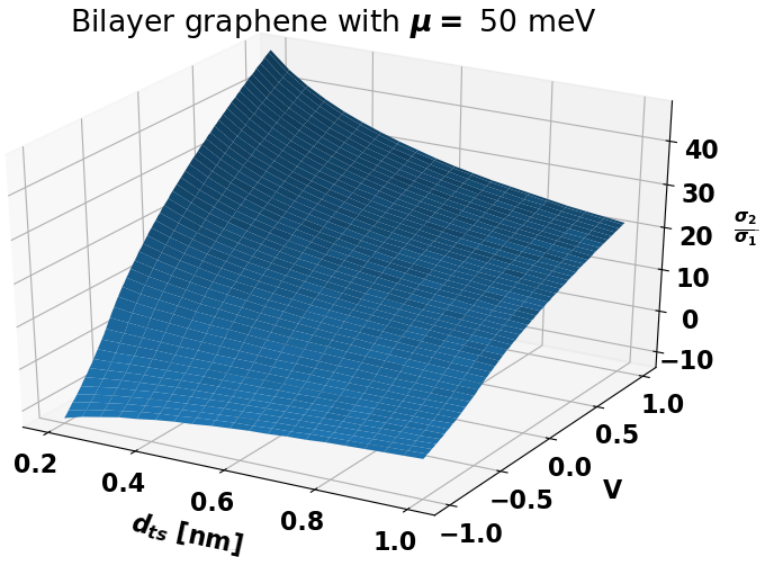

Figure 5.3: *Charge density distribution in a bilayer graphene system as a function of bias voltage and tip- sample distance. In this calculation, μ = 50 meV.*

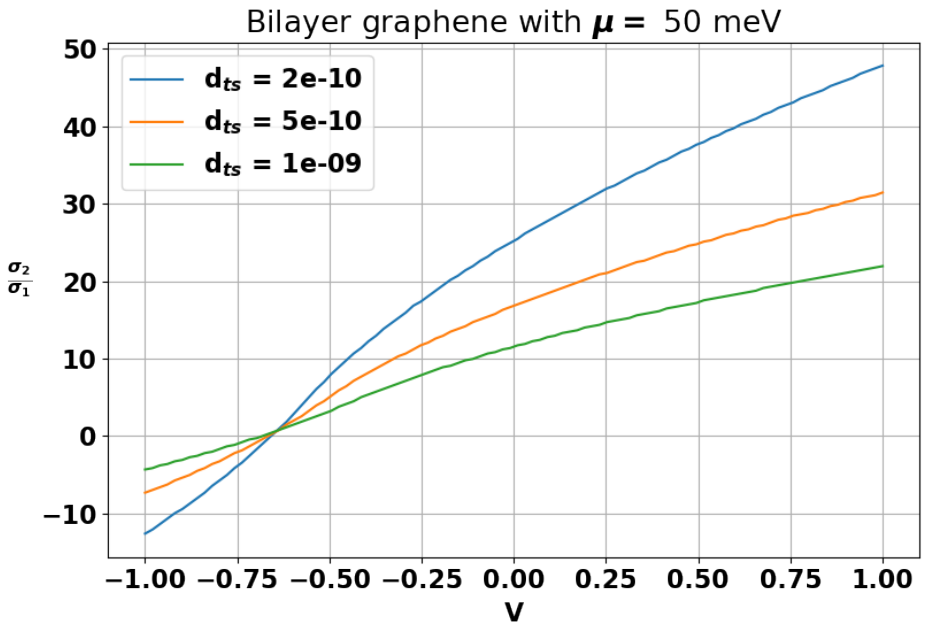

Figure 5.4: *Charge density distribution in a bilayer graphene system as a function of bias voltage. The different colors correspond to different tip-sample distances. In this calculation, μ = 50 meV.*

From the result displayed in the figures above, we can conclude that the STM tip significantly alters the charge distribution over the two graphene sheets. Notice that even if the bias is switched off, the tip still influences the charge distribution. This is a direct result of the work function difference between the probe tip and graphene. In figure 5.4, the different curves appear to cross near $V \approx$ -0.65 V. This value corresponds to when the applied bias exactly compensates for the work function difference and the chemical potential.
In figure 5.5, we plot the charge distribution as a function of bias voltage for varying the chemical potentials. As described above, $u_1 - \mu$ is fixed by the substrate, and therefore, sample dependent.

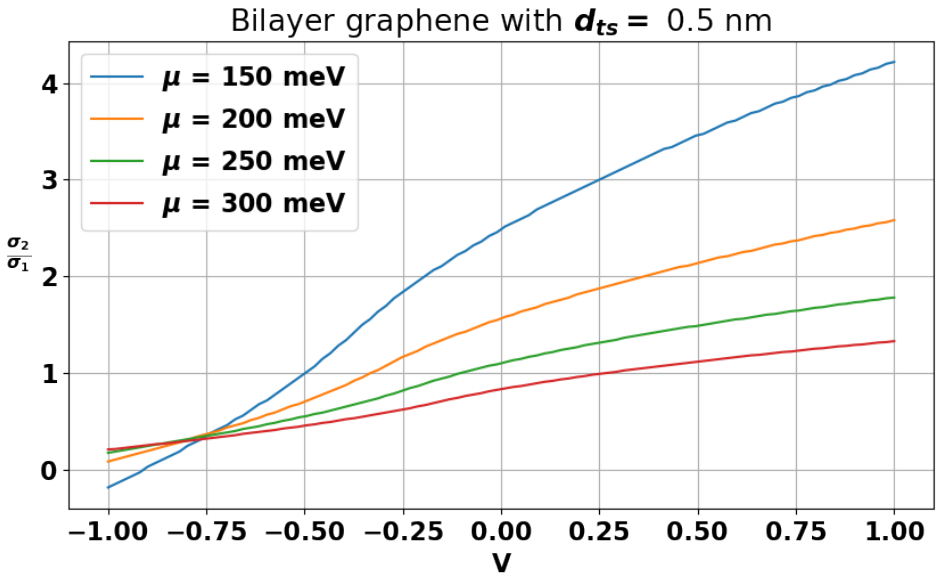

Figure 5.5: *Charge density distribution in a bilayer graphene system as a function of bias voltage. The different colors correspond to different values for the chemical potential. In this calculation,* $d_{ts} = 5$ *Å.*

Figure 5.5 shows that the charge distribution is altered significantly with μ. From this, we can draw a number of conclusions. First, because the model is heavily dependent on this value, exact knowledge of it is extremely significant for the accuracy of the predicted charge distribution. Second, to control the distribution of charge across the layers, the use of a backgate would be extremely beneficial. Its electric field could independently control the value of μ, thereby altering the influence of the probe tip. Third, this implies that STM is significantly more invasive in bilayer graphene on hBN, as compared to few-layer graphene on SiC owing to the difference in available free carriers.
Finally, we would like to point out another significant uncertainty in this model: The work function difference between the tip and graphene. Especially the work function of the tip can vary from tip to tip, and is therefore a major uncertainty in the model. On top of that, it is known that the work function of graphene is dependent on the charge density [25], a phenomenon that is not accounted for in this model.

5.4 TIBB in gated graphene samples

To conclude this chapter, we want to draw attention to a double gate model described in the work of Brar *et al.*. In this paper, an STM study is presented of Co adatoms on graphene. Graphene/SiO_2 devices are studied, and a model is presented for calculating the local shift in chemical potential under the STM tip. A schematic drawing of the system is displayed in figure 5.6. Because superconductivity in the MA-TBG system can only be realized by electrostic doping, we believe it is relevant to discuss this model, because it can potentially be modified with relative ease to describe the MA-TBG system during an STM experiment.

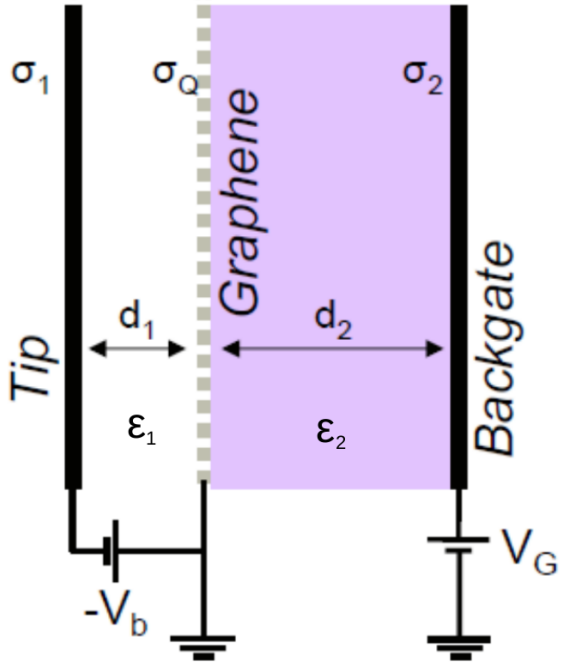

Figure 5.6: *Schematic of the model representing the tip- sample junction for estimating the effect of TIBB. The tip and sample are modeled as two infinite plates, a distance d1 and d_2 removed from the graphene flake respectively. We indicate the permittivity of the medium between the tip and the graphene as ϵ_1, and the medium between the backgate and the graphene as ϵ_2. The bias- and gate voltage are indicated with V_b and V_G respectively. The charge distribution on the tip, gate, and graphene are finally indicated as σ_1, σ_2, and σ_Q respectively.*

The tip, graphene, and the backgate form a triple plate capacitor. Because of the quantum capacitance of graphene, a finite potential difference, ϕ_Q is present in the layer itself when a charged electrode is brought in close

Version of November 25, 2018– Created November 25, 2018 - 02:09

proximity (in this case, the tip). Since the graphene is grounded however, this implies that the total chemical potential is zero. Therefore, the local shift in chemical potential due to the presence of the tip, is given by:

$$\Delta\mu = -e\phi_Q \tag{5.14}$$

ϕ_Q can be calculated by considering the total energy of the system:

$$E_{tot} = \frac{d_1\sigma_1^2}{\epsilon_1} + \frac{d_2\sigma_2^2}{\epsilon_2} + \frac{4}{3}\hbar v_f\sqrt{\pi}\left(\frac{1}{e}\right)^{\frac{3}{2}}\frac{\sigma_Q^2}{\sqrt{|\sigma_Q|}} \tag{5.15}$$

In this expression, the first two terms correspond to the geometrical capacitance between the tip and graphene, and the backgate and graphene respectively. The third term accounts for the quantum capacitance of the graphene sheet, a direct result of the low carrier density in the material, and the quantum mechanical nature of electrons (ref [27]). After minimizing with respect to the charge densities (see reference [27]), a relation between the electrostatic potentials can be obtained. The result is:

$$\frac{d_1e^3}{\pi(\hbar v_f)^2\epsilon_1}|\phi_Q|\phi_Q + \left(1 + \frac{d_1\epsilon_2}{d_2\epsilon_1}\right)\phi_Q - \left(\phi_{tip} + \frac{d_1\epsilon_2}{d_2\epsilon_1}\phi_{gate}\right) = 0 \tag{5.16}$$

In this expression, ϕ_{tip} is given by the work function difference between the tip and graphene, and ϕ_{gate}, the work function of Si. We take all relevant parameters equal to the values we set in the previous sections. ϵ_1 is chosen equal to the vacuum permittivity, ϵ_0. ϵ_2 is chosen as $3.8\epsilon_0$, the permittivity of SiO_2. Furthermore, d_1 and d_2 are set to 5 Å and 200 nm respectively. Finally, the shift in chemical potential can be calculated by solving for ϕ_Q. The result is plotted in figure 5.7.

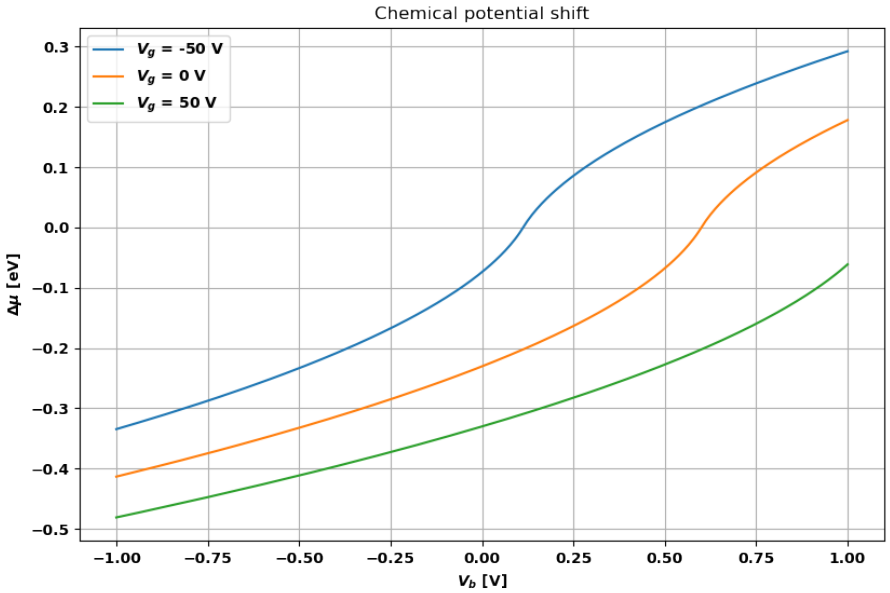

Figure 5.7: *Chemical potential shift due to the presence of the STM tip, as calculated by the model described above. The different colored curves correspond to different backgate voltages.*

From this result, we can conclude that the chemical potential is influenced, both by the bias- and the gate voltage. It is however unclear how this shift influences the emergent superconductivity in the MA-TBG system. To say something more about this, experimental results will be necessary. The reason for this is that it is so far unclear what the physical origin is of the observed phenomenon.

Chapter 6

Summary and Outlook

In this work, we developed and fabricated a dummy sample for testing capacitive navigation in a standard STM setup. Aimed at ultimately conducting STM measurements on graphene flakes, we calculate the effect of a biased STM tip on the charge distribution in a graphene bilayer. We also estimate the chemical potential shift in a gated graphene sample as a result of the probe tip. All results unambiguously suggest that the STM tip will strongly influence the electrical behavior of the graphene system. Unfortunately, it is not quite possible to quantify the effect on phenomena such as the observed superconductivity in MA-TBG, because their physical origin is still unclear.

Moving forward, we will further attempt to quantify the effect of charge redistribution and TIBB in the graphene bilayer as a result of the STM tip. We plan to combine the two models investigated above to estimate the shift in chemical potential in a gated bilayer system, also taking into account the quantum capacitance of the graphene sheets. Furthermore, very recently, it was observed with ARPES that charge inhomogeneity in bilayer graphene can create extremely flat bands (reference [28]). Since we have seen from this work that this parameter is freely tunable with the STM tip (wanted or unwanted), we believe it is definitely worth investigating the effects of charge inhomogeneity in a bilayer system.

In parallel, we strive to get the STM setup functional again. After that, we plan to test the capacitive navigation using the dummy sample fabricated in this work.

References

[1] Y. Cao, V. Fatemi, A. Demir, S. Fang, S. L. Tomarken, J. Y. Luo, J. D. Sanchez-Yamagishi, K. Watanabe, T. Taniguchi, E. Kaxiras, R. C. Ashoori, and P. Jarillo-Herrero, *Correlated insulator behaviour at half-filling in magic-angle graphene superlattices*, Nature **556**, 80 (2018).

[2] Y. Cao, V. Fatemi, S. Fang, K. Watanabe, T. Taniguchi, E. Kaxiras, and P. Jarillo-Herrero, *Unconventional superconductivity in magic-angle graphene superlattices*, Nature **556**, 43 (2018).

[3] P. R. Wallace, *The band theory of graphite*, Physical Review **71**, 622 (1947).

[4] A. H. C. Neto, F. Guinea, N. M. R. Peres, K. S. Novoselov, and A. K. Geim, *The electronic properties of graphene*, Reviews of Modern Physics **81**, 109 (2009).

[5] K. S. Novoselov, A. K. Geim, S. V. Morozov, D. Jiang, M. I. Katsnelson, I. V. Grigorieva, S. V. Dubonos, and A. A. Firsov, *Two-dimensional gas of massless Dirac fermions in graphene*, Nature **438**, 197 (2005).

[6] F. Guinea, A. H. Castro Neto, and N. M. Peres, *Electronic states and Landau levels in graphene stacks*, Physical Review B - Condensed Matter and Materials Physics **73**, 1 (2006).

[7] R. Bistritzer and A. H. MacDonald, *Moire bands in twisted double-layer graphene*, PNAS **108**, 12233 (2010).

[8] B. Keimer, S. A. Kivelson, M. R. Norman, S. Uchida, and J. Zaanen, *From quantum matter to high-temperature superconductivity in copper oxides*, Nature **518**, 179 (2015).

[9] I. Battisti, K. M. Bastiaans, V. Fedoseev, A. De La Torre, N. Iliopoulos, A. Tamai, E. C. Hunter, R. S. Perry, J. Zaanen, F. Baumberger, and

M. P. Allan, *Universality of pseudogap and emergent order in lightly doped Mott insulators*, Nature Physics **13**, 21 (2017).

[10] L. De Medici, G. Giovannetti, and M. Capone, *Selective Mott physics as a key to iron superconductors*, Physical Review Letters **112**, 1 (2014).

[11] G. Binnig and H. Rohrer, *Scanning tunneling microscopy*, Surface Science **126**, 236 (1983).

[12] R. Young, J. Ward, and F. Scire, *The Topografiner : An Instrument for Measuring Surface Microtopography Principle of Operation*, **999** (1972).

[13] J. Bardeen, *Tunnelling from a many-particle point of view*, Physical Review Letters **6**, 57 (1961).

[14] J. Tersoff and D. Hamann, *Theory and application for the scanning tunneling microscope*, Physical review letters **50**, 1998 (1983).

[15] J. Tersoff and D. R. Hamann, *Theory of the scanning tunneling microscope*, Physical Review B **31**, 805 (1985).

[16] Y. Zhao, J. Wyrick, F. D. Natterer, J. F. Rodriguez-Nieva, C. Lewandowski, K. Watanabe, T. Taniguchi, L. S. Levitov, N. B. Zhitenev, and J. A. Stroscio, *Creating and probing electron whispering-gallery modes in graphene*, Science **348**, 672 (2015).

[17] F. Ghahari, D. Walkup, C. Gutiérrez, J. F. Rodriguez-Nieva, Y. Zhao, J. Wyrick, F. D. Natterer, W. G. Cullen, K. Watanabe, T. Taniguchi, L. S. Levitov, N. B. Zhitenev, and J. A. Stroscio, *An on/off Berry phase switch in circular graphene resonators*, Science **356**, 845 (2017).

[18] I. Battisti, G. Verdoes, K. van Oosten, K. M. Bastiaans, and M. P. Allan, *Definition of design guidelines, construction and performance of an ultra-stable scanning tunneling microscope for spectroscopic imaging*, arXiv:1810.09727 .

[19] G. Li, A. Luican, and E. Y. Andrei, *Self-navigation of a scanning tunneling microscope tip toward a micron-sized graphene sample*, Review of Scientific Instruments **82** (2011).

[20] J. N. Longschamp, C. Escher, and H. W. Fink, *Ultra-Clean Freestanding Graphene by Platinum-Metal Catalysis*, arXiv:1210.6824 .

[21] V. W. Brar, R. Decker, H. M. Solowan, Y. Wang, L. Maserati, K. T. Chan, H. Lee, Ç. O. Girit, A. Zettl, S. G. Louie, M. L. Cohen, and M. F. Crommie, *Gate-controlled ionization and screening of cobalt adatoms on a graphene surface*, Nature Physics **7**, 43 (2011).

[22] G. J. De Raad, D. M. Bruls, P. M. Koenraad, and J. H. Wolter, *Interplay between tip-induced band bending and voltage-dependent surface corrugation on GaAs(110) surfaces*, Physical Review B - Condensed Matter and Materials Physics **66**, 1 (2002).

[23] R. M. Feenstra, Y. Dong, M. P. Semtsiv, and W. T. Masselink, *Influence of tip-induced band bending on tunnelling spectra of semiconductor surfaces*, Nanotechnology **18** (2007).

[24] Z. Zhang and J. T. Yates, *Band bending in semiconductors: Chemical and physical consequences at surfaces and interfaces*, **112**, 5520 (2012).

[25] H. Min, S. Adam, Y. J. Song, J. A. Stroscio, M. D. Stiles, and A. H. MacDonald, *Landau levels and band bending in few-layer epitaxial graphene*, Physical Review B - Condensed Matter and Materials Physics **83**, 1 (2011).

[26] D. Sun, C. Divin, C. Berger, W. A. De Heer, P. N. First, and T. B. Norris, *Spectroscopic measurement of interlayer screening in multilayer epitaxial graphene*, Physical Review Letters **104**, 24 (2010).

[27] S. Luryi, *Quantum capacitance devices*, Applied Physics Letters **52**, 501 (1988).

[28] D. Marchenko, D. V. Evtushinsky, E. Golias, A. Varykhalov, T. Seyller, and O. Rader, *Extremely flat band in bilayer graphene*, Science Advances **1**, 59 (2018).